FFI RAPPORT

SPECTRAL ELEMENT BENCHMARK SIMULATIONS OF NATURAL CONVECTION IN TWO-DIMENSIONAL CAVITIES

GJESDAL Thor, WASBERG Carl Erik, REIF Bjørn Anders Pettersson

FFI/RAPPORT-2004/00590

SPECTRAL ELEMENT BENCHMARK SIMULATIONS OF NATURAL CONVECTION IN TWO-DIMENSIONAL CAVITIES

GJESDAL Thor, WASBERG Carl Erik, REIF Bjørn
Anders Pettersson

FFI/RAPPORT-2004/00590

FORSVARETS FORSKNINGSINSTITUTT
Norwegian Defence Research Establishment
P O Box 25, NO-2027 Kjeller, Norway

FORSVARETS FORSKNINGSINSTITUTT (FFI)
Norwegian Defence Research Establishment

P O BOX 25
N0-2027 KJELLER, NORWAY

UNCLASSIFIED

SECURITY CLASSIFICATION OF THIS PAGE
(when data entered)

REPORT DOCUMENTATION PAGE

1) PUBL/REPORT NUMBER	2) SECURITY CLASSIFICATION	3) NUMBER OF PAGES
FFI/RAPPORT-2004/00590	UNCLASSIFIED	28
1a) PROJECT REFERENCE	**2a) DECLASSIFICATION/DOWNGRADING SCHEDULE**	
FFI-V/820/170	-	

4) TITLE

SPECTRAL ELEMENT BENCHMARK SIMULATIONS OF NATURAL CONVECTION IN TWO-DIMENSIONAL CAVITIES

5) NAMES OF AUTHOR(S) IN FULL (surname first)

GJESDAL Thor, WASBERG Carl Erik, REIF Bjørn Anders Pettersson

6) DISTRIBUTION STATEMENT

Approved for public release. Distribution unlimited. (Offentlig tilgjengelig)

7) INDEXING TERMS

IN ENGLISH:	IN NORWEGIAN:
a) Natural convection	a) Naturlig konveksjon
b) 8:1 thermally driven cavity	b) 8:1 termisk drevet kavitet
c) Incompressible flow	c) Inkompressibel strømning
d) Spectral element method	d) Spektralelementmetode
e) Operator splitting	e) Operatorsplitting

THESAURUS REFERENCE:

8) ABSTRACT

This report presents the results of spectral element simulations of natural convection in two-dimensional cavities. In particular, a detailed comparison is performed with the reference data recently described by Christon *et. al.* [*Int .J. Numer. Meth. Fluids*, vol. 40, pp. 953-980, 2002]. The Navier-Stokes equations augmented by the Boussinesq approximation to represent buoyancy effects are solved by a numerical method based on spectral element discretisations and operator splitting. The computed results agree closely with the reference data for both the square and the rectangular cavity configurations.

9) DATE	AUTHORIZED BY This page only	POSITION
2004-02-23	Bjarne HAUGSTAD	Director of Research

ISBN-82-464-0842-9

UNCLASSIFIED

SECURITY CLASSIFICATION OF THIS PAGE
(when data entered)

CONTENTS

Page

SPECTRAL ELEMENT BENCHMARK SIMULATIONS OF NATURAL CONVECTION IN TWO-DIMENSIONAL CAVITIES

1 INTRODUCTION

The development and application of higher-order numerical schemes for fluid flow computations has become an increasingly important activity. The primary reason for this is that computational fluid dynamical (CFD) analyses are becoming an integral part of the design cycle in an increasing number of industries. As the number of applications is growing, however, the number of complex configurations that need to be predicted is also increasing. More sophisticated turbulence models are therefore needed to predict the flow phenomena that arise.

We are developing a parallelised two- and three-dimensional Navier-Stokes and Boussinesq spectral element solver for incompressible fluid flow computations. The ultimate objective of this development is two-fold. Firstly to conduct benchmark simulations by means of highly accurate direct numerical simulations to support our ongoing efforts in turbulence physics research. Secondly, to develop models for large-eddy simulations in an environment where the numerical errors are very small such that the true performance of the model can be revealed.

In this paper we consider a two-dimensional cavity where the flow is driven by the natural convection set up by differentially heated walls. The thermal cavity flow is an important prototype flow for a wide range of practical technological problems, including ventilation, crystal growth in liquids, nuclear reactor safety, and the design of high-powered laser systems. Cavity flows are furthermore often used as test cases for code verification and validation because they are simple to set up and reliable reference solutions are readily available. Although the flow configuration is two-dimensional, thermal cavity flows display a plethora of interesting fluid dynamic phenomena and complex features such as impinging boundary layers, stratification and an intricate temporal behaviour. Since these effects depend strongly on the cavity aspect ratio, thermal boundary conditions and Prandtl number, this test case constitutes a severe challenge for numerical schemes.

The motivation of this study is to assess the numerical accuracy of the code in a well documented case. After a brief revisit to the classical steady state configuration of the square cavity [1, 2], we address the slightly supercritical time-dependent flow in a tall cavity with aspect ratio 8:1. This configuration was the subject on a recent workshop reported by Christon *et al.* [3] in which a total of 31 solutions were submitted for this problem. The numerical method we employ differ in two respects from those represented at the workshop; the spectral element discretisation and a time integration method based on an operator splitting of the advection-diffusion equations for momentum and temperature. As such, the present work supplements the results presented previously and extends the data

base of results for this particular benchmark case.

In addition to presenting a 'best' solution to demonstrate the accuracy of the method, we study the impact of computational parameters such as the computational grid, time-step, and numerical tolerance parameters on the quality of the computed solutions, as well as the effect of the spatial filtering procedure developed by Fischer and Mullen [4] to reduce aliasing errors.

2 NUMERICAL METHOD

The equations describing the Boussinesq approximation for the dynamics of a viscous, incompressible fluid affected by buoyancy forces are

$$\nabla \cdot \mathbf{u} = 0, \tag{2.1a}$$

$$\frac{\partial \mathbf{u}}{\partial t} + \mathbf{u} \cdot \nabla \mathbf{u} = -\nabla p + \nu \nabla^2 \mathbf{u} + \beta \left(T - T_{\mathrm{ref}}\right) \mathbf{g}, \tag{2.1b}$$

$$\frac{\partial T}{\partial t} + \mathbf{u} \cdot \nabla T = \alpha \nabla^2 T, \tag{2.1c}$$

where $\mathbf{u} = (u, v)$ represents the velocity, p represents the pressure, and T represents the temperature. The kinematic viscosity is denoted by ν, the thermal diffusivity by α, the coefficient of thermal expansion by β, and the gravitational acceleration $\mathbf{g}$. The Boussinesq approximation is valid provided that the density variations, $\rho(T)$, are small; in practice this means that that only small temperature deviations from the mean temperature are admitted.

The relevant non-dimensional parameters that characterize the flow are:

- The Prandtl number; $\mathrm{Pr} = \nu/\alpha$,
- the Reynolds number; $\mathrm{Re} = UL/\nu$, and
- the Rayleigh number; $\mathrm{Ra} = g\beta\Delta T L^3/\nu\alpha$.

Note that the free convection cases we consider below are completely determined by the Prandtl and Rayleigh numbers.

The key to an efficient and accurate solution of the Boussinesq/Navier-Stokes system (2.1) is a judicious use of implicit-explicit splitting for terms of different character. In particular, if the advection-diffusion equations are solved by an implicit-explicit procedure, the temperature equation can be decoupled from the remaining momentum equations. The buoyancy source term can then be calculated first and fed directly to the Navier-Stokes solver. In addition to the diffusive terms, we also treat the pressure term and the divergence equation implicitly.

In the temporal discretisation based on the implicit-explicit time splitting we treat the advection-diffusion equations for the temperature and the velocities according to the

operator-integration-factor (OIF) method of Maday *et al.* [5]. The advective terms are integrated explicitly by an adaptive second-order accurate Runge-Kutta method, while the viscous terms are integrated by the implicit second order backward difference scheme (BDF2), given by

$$\frac{\partial u}{\partial t} = \frac{3u^{n+1} - 4u^n + u^{n-1}}{2\Delta t} + O(\Delta t^2).$$

After discretisation in time we can write (2.1) in the form

$$\frac{3T^{n+1} - 4T^n + T^{n-1}}{2\Delta t} - \alpha\nabla^2 T^{n+1} = f_T\left((\mathbf{u}\cdot\nabla T)^n, (\mathbf{u}\cdot\nabla T)^{n-1}, \dots\right), \tag{2.2a}$$

$$\frac{3\mathbf{u}^{n+1} - 4\mathbf{u}^n + \mathbf{u}^{n-1}}{2\Delta t} - \nu\nabla^2\mathbf{u}^{n+1} = -\nabla p + f_{\mathbf{u}}(\mathbf{u}^n, \mathbf{u}^{n-1}, \dots) + \beta\left(T - T_{\text{ref}}\right)\mathbf{g}, \tag{2.2b}$$

$$\nabla\cdot\mathbf{u}^{n+1} = 0, \tag{2.2c}$$

in which the explicit treatment of the advection term is included in the source terms f_T and $f_{\mathbf{u}}$. Note that we have changed the ordering of the equations in (2.2) to emphasize that the temperature at the new time level, T^{n+1}, can be obtained from known velocity data.

The spatial discretisation is based on a spectral element method [6, 7]; the computational domain is sub-divided into non-overlapping quadrilateral (in 2D) or hexahedral (in 3D) cells or elements. Within each element, a weak representation of (2.2) is discretised by a Galerkin method in which we choose the test and trial functions from bases of polynomial spaces, i.e.

$$u_i^h \in P_N(x)\otimes P_N(y)\otimes P_N(z), \tag{2.3a}$$

$$p^h \in P_{N-2}(x)\otimes P_{N-2}(y)\otimes P_{N-2}(z), \tag{2.3b}$$

where $P_N(x)$ denotes the function space spanned by polynomials of degree N. Note that we employ a lower order basis for the pressure spaces to avoid spurious pressure modes in the solution [7]. The velocity variables are C^0-continuous across element boundaries and they are represented at the Gauss-Lobatto-Legendre (GLL) points for the numerical integration, whereas the pressure variable is discontinuous across element boundaries and are represented at the interior Gauss-Legendre (GL) points. The one-dimensional polynomial basis functions, $h_j(\xi)$, are defined as the Lagrange interpolants that vanish at all but one of the Gauss-Lobatto-Legendre and Gauss-Legendre points, respectively, such that

$$h_j(\xi_i) = \delta_{ij}, \tag{2.4}$$

where ξ_i represents the GLL or GL grid point positions.

The GLL grid corresponding to the Legendre polynomial of degree N has $(N+1)$ points. Gauss-Lobatto-Legendre quadrature at the $(N+1)$ GLL points is exact for polynomial of degree $(2N-1)$. Hence, the computation of the inner products corresponding to the

diffusive terms in (2.1) are calculated exactly, whereas the evaluation of the non-linear advective terms incurs quadrature (aliasing) errors. These errors can be detrimental to the stability of the method and must be controlled. The most fundamental approach to de-aliasing is to perform over-integration [8, 9] – that is, to over-sample and to use more quadrature points to evaluate the inner products containing non-linear terms. An computationally more efficient alternative approach is to use polynomial filtering of the solutions as proposed by Fischer and Mullen [4]. The filtering comprises a weighted sum of the original unfiltered field, u_N and its projection onto the space of polynomials of degree $N-1$. If I_n^m is the interpolation operator from the n-point to the m-point Gauss-Lobatto-Legendre grid, the one-dimensional projection operator can be written $\Pi_{N-1} = I_{N-1}^N I_N^{N-1}$, and the filter is defined by.

$$F_\eta \equiv \eta\Pi_{N-1} + (1-\eta)I, \tag{2.5}$$

where η is a filter parameter. Higher dimensional filter functions are constructed by tensor products of the one-dimensional filter.

For the spatial discretization of the Boussinesq/Navier-Stokes system (2.1), we introduce the discrete Helmholtz operator,

$$H_\epsilon = \kappa B + \epsilon A,$$

where A and B are the stiffness- and mass matrices in d spatial dimensions, $\kappa = 3/2\Delta t$ is a time discretization parameter, and ϵ is the diffusivity coefficient. Further, let G and $D = G^T$ denote the discrete gradient and divergence operators, respectively. Appropriate boundary conditions are included in these discrete operators. This gives the discrete equations

$$H_\alpha T^{n+1} = Bf_T(\mathbf{u}^n, T^n, \mathbf{u}^{n-1}, T^{n-1}, \dots), \tag{2.6a}$$
$$H_\nu \mathbf{u}^{n+1} - Gp^{n+1} = Bf_{\mathbf{u}}(\mathbf{u}^n, \mathbf{u}^{n-1}, \dots, T^{n+1}), \tag{2.6b}$$
$$-D\mathbf{u}^{n+1} = 0. \tag{2.6c}$$

Note that the change of sign in the pressure gradient term in (2.6b) is caused by an integration by parts in the construction of the weak form of the problem. The temperature equation is, as we noted above, essentially de-coupled from the momentum equation and can hence be solved separately. The remaining dependent variables, velocities and pressure, are computed efficiently by a second order accurate pressure correction method [10, 11] that can be written [12, 13]

$$Hu^* = Bf + Gp^n, \tag{2.7a}$$
$$DQG(p^{n+1} - p^n) = -Du^*, \tag{2.7b}$$
$$u^{n+1} = u^* + QG(p^{n+1} - p^n), \tag{2.7c}$$

where u^* is an auxiliary velocity field that not necessarily satisfies the continuity equation $Du^* = 0$.

The discrete Helmholtz operator is symmetric and diagonally dominant, since the mass matrix of the Legendre discretisation is diagonal, and can be efficiently solved by the

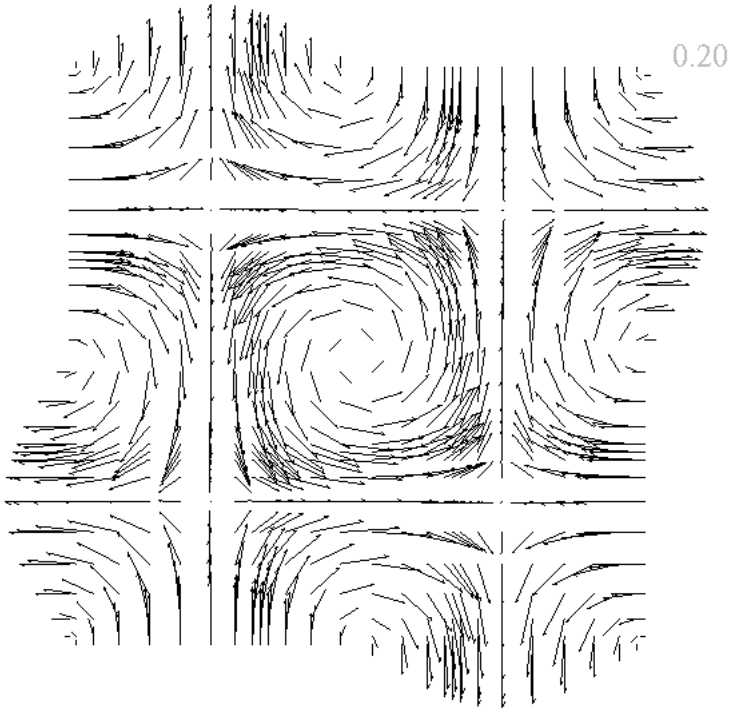

Figure 3.1: Computed velocity field at $t = 0.2$ for the Taylor vortices (3.1).

conjugate gradient method with a diagonal (Jacobi) preconditioner. Whereas the pressure operator DQG is easily computed; it is ill-conditioned. The pressure system is solved by the preconditioned conjugate gradient method, with a multilevel overlapping Schwarz preconditioner [14].

3 VERIFICATION OF THE NAVIER-STOKES SOLVER

In this section we present a verification of the Navier-Stokes solver in an isothermal case. As the test problem we use the *Taylor vortices* [15], an exact analytical solution of the two-dimensional Navier-Stokes equations in which all variables have non-trivial solutions:

$$\begin{aligned} u &= -\cos(\pi x)\sin(\pi y)e^{-2\pi^2\nu t}, \\ v &= \sin(\pi x)\cos(\pi y)e^{-2\pi^2\nu t}, \\ p &= -\frac{1}{4}\left[\cos(2\pi x)+\cos(2\pi y)\right]e^{-4\pi^2\nu t}. \end{aligned} \tag{3.1}$$

Although this example is artificially constructed, such that the pressure gradient balances the convective terms and the unsteady terms balance the diffusion, it is useful because both spatial and temporal accuracy in all variables can be checked simultaneously. The exact velocity field is used as initial condition, and the boundary conditions are either periodic, or time-dependent Dirichlet conditions. The velocity field at $t = 0.2$ is shown in Fig. 3.1.

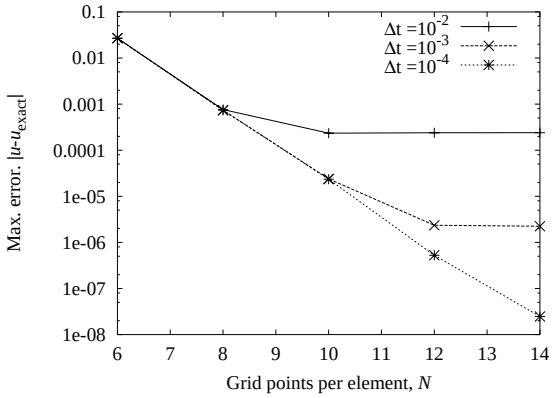

Figure 3.2: Grid convergence (p-refinement) in u for the Taylor vortices (3.1). Computed solutions at $t = 1$ using $M = 2 \times 2$ elements.

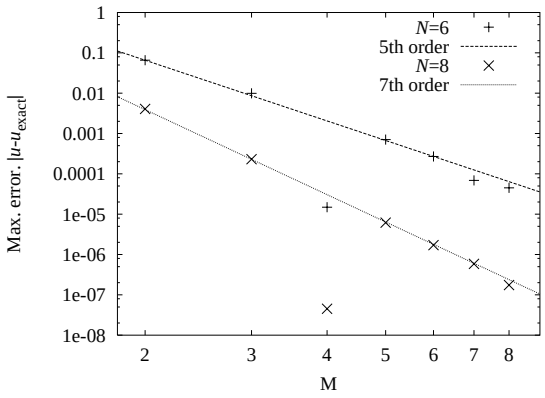

Figure 3.3: Grid convergence (h-refinement) in u for the Taylor vortices (3.1). Computed solutions at $t = 0.2$ using $N \times N$ grid points in each element.

We performed grid convergence studies by independently increasing the number of grid points, N, per element (p-refinement) and the number of elements, M (h-refinement). Fig. 3.2 shows the grid convergence results for p-refinement. As expected, we observe exponential convergence when N increases to the point where time-integration errors dominate. Furthermore, we show in Fig. 3.3 that we obtain algebraic convergence for h-refinement (i.e. constant N and increasing M). Hence, for a fixed N the spectral element method converges similarly to a finite element method of order $(N - 1)$.

We then consider the time accuracy of the computed solutions. The time integration method includes two operator splitting methods; the OIF splitting of advective and diffusive terms and the pressure correction method to compute the velocity and pressure. We performed computations in which we only employed the OIF splitting and solved the velocity-pressure coupling by an exact block LU-decomposition of the discretised Stokes problem known as the Uzawa method, and computations in which we used both splittings. In both cases the method is indeed second-order accurate in the implicit time step, Δt, as we show in

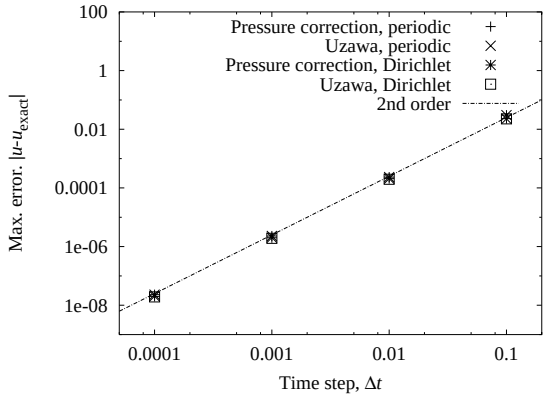

Figure 3.4: Δt-convergence for the Taylor vortices (3.1). Computed solutions at $t = 0.2$ with $M = 4 \times 4$ elements and $N = 12 \times 12$ points in each element.

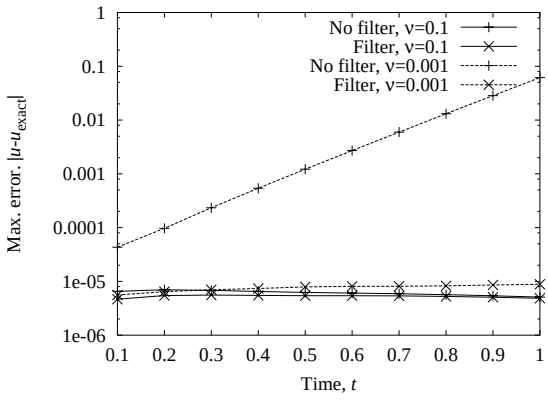

Figure 3.5: Effect of filtering on error growth, dependence on ν. $M = 3 \times 3$ elements, $N = 10 \times 10$ points per element, filter parameter $\eta = 0.05$.

Fig. 3.4.

Finally, we investigate the effect of employing the filter, given by Eq. (2.5), proposed by Fischer and Mullen [4]. We compare the time evolution of the errors for filtered and unfiltered simulations, respectively. In the filtered computations, the filter parameter was set to $\eta = 0.05$. In Fig. 3.5 we can observe that the error in the unfiltered calculations grows exponentially in time for small viscosity, and that this growth occurs already from the start of the calculation on a coarse grid. For refined grids, the effects of this error growth is felt at a later time as shown in Fig. 3.6. In both figures we observe that application of the filter eliminates the unphysical error growth.

The spatial convergence of the filtered calculations is depicted in Fig. 3.7, where exponential convergence is observed in both the filtered and non-filtered case. When the accuracy is limited by the spatial resolution, the errors are however several orders of magnitude smaller when filtering is employed.

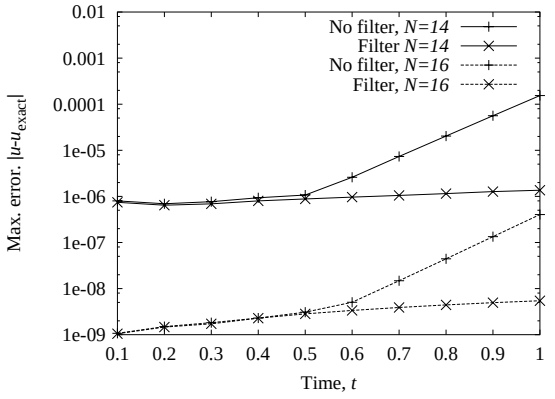

Figure 3.6: Effect of filtering on error growth, dependence on N. $M = 3 \times 3$, $\nu = 10^{-3}$, $\eta = 0.05$.

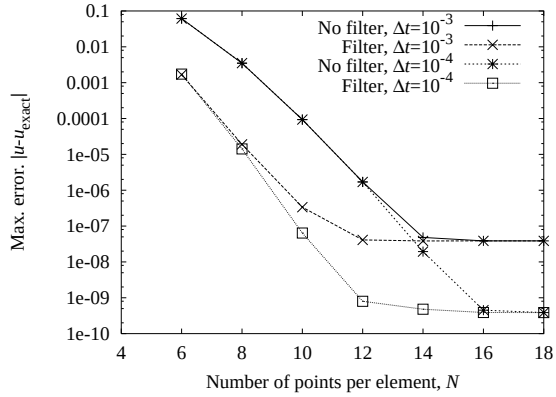

Figure 3.7: Effect of filtering on the grid convergence (p*-refinement) for the Taylor vortices (3.1). Computed solutions at* $t = 0.2$, $M = 3 \times 3$, $\nu = 10^{-3}$, $\eta = 0.5$.

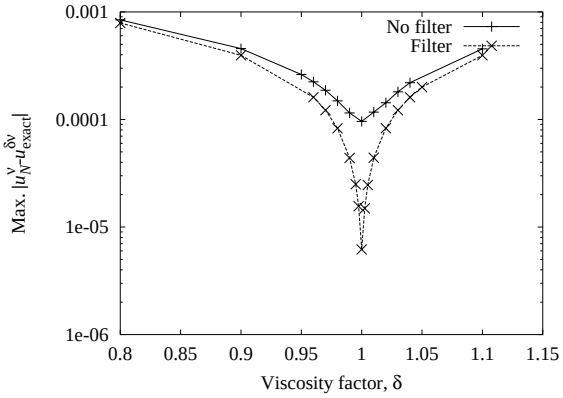

Figure 3.8: Maximum of $u_N^\nu - u_{\text{exact}}^{\delta\nu}$ for the Taylor vortices (3.1), as function of β, with and without filtering with $\eta = 0.05$. 3×3 elements, 10×10 grid points in each element, $\nu = 10^{-3}$, $\Delta t = 10^{-4}$, $t = 0.2$.

To establish whether the additional dissipation induced by the filtering actually has the same effect as increasing the viscosity ν, thus lowering the Reynolds number, we compared the computed solution for $M = 3$, $N = 10$, $\nu = 10^{-3}$, $\eta = 0.05$, at $t = 0.2$ against the exact solutions based on a scaled viscosity $\delta\nu$ where δ is a scaling factor close to unity. The results are shown in Fig. 3.8, and shows that the method with filtering does indeed solve the equations at the correct Reynolds number, and moreover that it performs significantly better than the non-filtered method.

We have also performed a similar verification of the three-dimensional implementation against a Beltrami flow, given in [16], that also have non-trivial solutions in all variables.

4 CAVITY SIMULATIONS

We have performed simulation of the free convection in two-dimensional square and rectangular cavities. The problem comprises a box of side length L_x and L_y filled with a Boussinesq fluid characterized by a Prandtl number, Pr=0.71. The vertical walls are kept at constant temperature T_{hot} and T_{cold}, respectively, while the horizontal lid and bottom are insulated with zero heat flux. The direction of gravity is downward, parallel to the heated walls. The cavity flow exhibits a centro-symmetric property [17] in that, for the steady-state base flows, the velocity and temperature fields are skew-symmetric with respect to the diagonal of the cavity, whereas the unstable eigenmodes either share this skew-symmetry or have the opposite symmetry.

The most important diagnostic connected to the free convection cavity flow is the average Nusselt number, which expresses the non-dimensional heat flux across the cavity. The Nusselt number is usually calculated at a vertical line, typically the hot and the cold wall, or

Table 4.1: Computed Nusselt numbers for the square cavity compared to the extrapolated results of the reference solutions of de Vahl Davis (1983) and Hortmann et al. *(1990).*

Ra:	10^4	10^5	10^6
Present results:	2.24482	4.52164	8.82520
de Vahl Davis [1] :	2.243	4.519	8.800
Hortmann *et al.* [2]:	2.24475	4.52164	8.82513

as a global average over the entire cavity. The Nusselt number is given by

$$\mathrm{Nu} = \frac{Q}{Q_0}, \tag{4.1a}$$

where Q is the computed heat flux through the cavity

$$Q = \int_0^{L_y} \left(uT - \alpha \frac{\partial T}{\partial x} \right) dy, \qquad \text{or} \qquad Q = \int_0^{L_x} \int_0^{L_y} \left(uT - \alpha \frac{\partial T}{\partial x} \right) dx dy, \tag{4.1b}$$

for line and volume averages, respectively. The reference value, Q_0, is the corresponding heat flux if the heat transfer were by pure conduction

$$Q_0 = L_y \frac{\alpha \Delta T}{L_x}, \qquad \text{or} \qquad Q_0 = L_x L_y \frac{\alpha \Delta T}{L_x} = L_y \alpha \Delta T. \tag{4.1c}$$

4.1 Square cavity simulations

The steady-state differentially heated square cavity flow was the subject of one of the first benchmark comparison exercises, reported in de Vahl Davis and Jones [18]. The reference results produced in that exercise are given by de Vahl Davis [1]. The results of de Vahl Davis were produced, for Rayleigh numbers in the range 10^3–10^6, using a stream-function/vorticity formulation discretised by a second-order finite difference method on a regular mesh. Later, more accurate results obtained by a second order finite volume method on higher resolution non-uniform grids were presented by Hortmann *et al.* [2].

We performed simulations using $M = 4 \times 4$ elements varying the resolution in each element from $N = 6 \times 6$ to $N = 24 \times 24$. In Figs. 4.1–4.3 we show the grid convergence of the computed global Nusselt numbers compared to the previously reported benchmark results [1] and [2]. Note the excellent agreement with the reference data; even the coarsest resolution (i.e. 21×21 grid points) produces solutions that are essentially converged except at the largest Rayleigh number. In Table 4.1 we compare the Nusselt numbers obtained at the finest grid with the 'grid-independent' values from the reference solutions obtained by Richardson extrapolation.

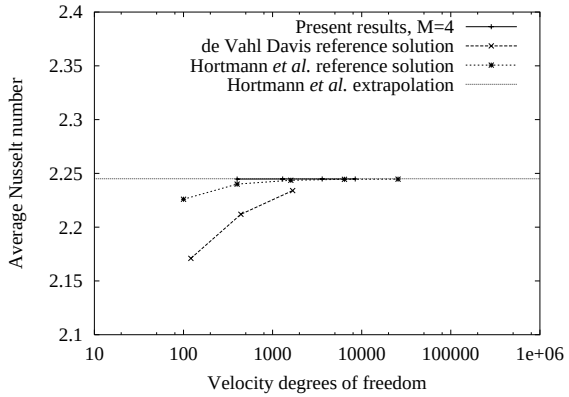

Figure 4.1: Grid convergence for the average Nusselt number for the square cavity simulation at $\mathrm{Ra} = 10^4$.

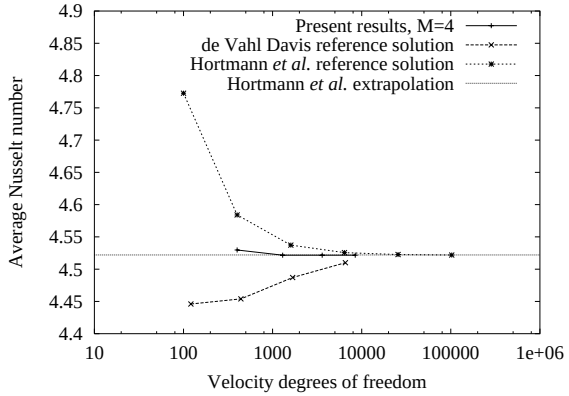

Figure 4.2: Grid convergence for the average Nusselt number for the square cavity simulation at $\mathrm{Ra} = 10^5$.

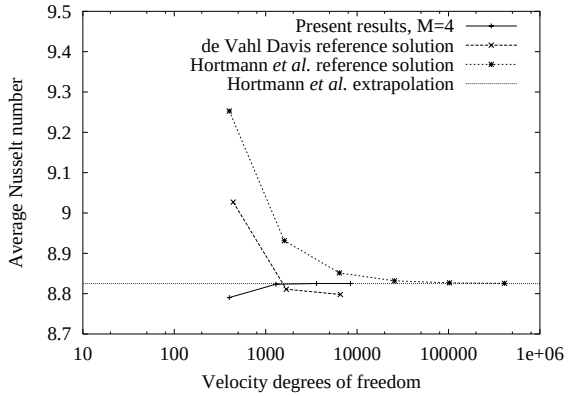

Figure 4.3: Grid convergence for the average Nusselt number for the square cavity simulation at $\mathrm{Ra} = 10^6$.

4.2 Tall cavity simulations

Christon *et al.* [3] summarise the results of a workshop discussing the free convection in a tall cavity with aspect ratio 8:1. The comparison was performed for a Rayleigh number $\mathrm{Ra} = 3.4 \times 10^5$ which is slightly above the transition point from steady-state to time-dependent flow at $\mathrm{Ra} \approx 3.1 \times 10^5$. A total of 31 solutions were submitted to the workshop, of these a pseudo-spectral solution, contributed by Xin and Le Quéré [19] using a spatial resolution of 48×180 modes was selected as the reference solution.

In addition to the wall and centre-line Nusselt number (4.1), we will employ several global and point measures of the solution for the comparison with the benchmark. The global velocity metric is related to the total kinetic energy and is given by

$$U = \sqrt{\frac{1}{2L_xL_y}\int_0^{L_x}\int_0^{L_y} \mathbf{u}\cdot\mathbf{u}\; dxdy}, \tag{4.2}$$

while the vorticity metric is

$$\Omega = \sqrt{\frac{1}{2L_xL_y}\int_0^{L_x}\int_0^{L_y} (v_x - u_y)^2\; dxdy}. \tag{4.3}$$

Furthermore point values for non-dimensional temperature, θ, velocity components, u and v, and vorticity, ω, were monitored at the location ($x_1 = 0.181 \times W$, $y_1 = 7.37 \times W$). The skew-symmetry of the solution was monitored by the skewness metric $\varepsilon_{12} = \theta(x_1, y_1) + \theta(x_2, y_2)$, where $x_2 = W - x_1$ and $y_2 = H - y_1$. Finally, we monitored two pressure differences in the flow; one across the top of the cavity (Δp_{14}), and one in the boundary layer along the hot wall (Δp_{35}). We employed spectral interpolation, using the GLL Lagrange interpolant functions, to compute the function values at the monitor locations. For each diagnostic variable we computed the mean value and peak-to-valley oscillation amplitudes by averaging over several periods after the flow reached a statistically steady state.

The computed results depend on the governing equations and the boundary conditions and the spatial and temporal resolution, given by the grid size and time step. Furthermore, several algorithmic parameters – such as the weight factor in the filter given by Eq. (2.5) and different tolerance parameters related to the iterative solvers and the adaptive time integration of the advective terms – influence the solution. We have investigated the sensitivity of the diagnostic variables to variations in several of these parameters, viz

- Grid size. We used a uniform $M = 4 \times 20$ element grid in all simulations, varying the number of points per element from $N = 6 \times 6$ up to $N = 18 \times 18$. The coarsest grid we employed thus comprised 21×101 velocity grid points, whereas the finest grid had 69×341 points.
- Time step, Δt.

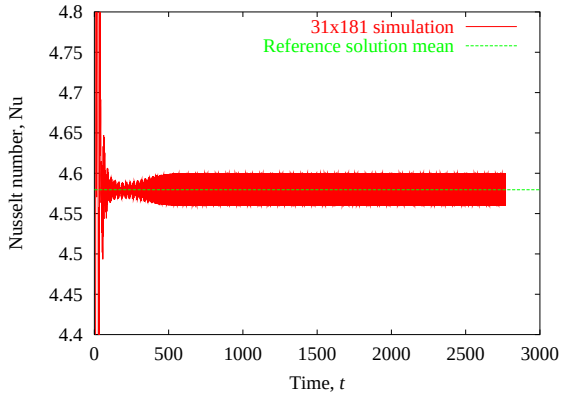

Figure 4.4: Time evolution of the global Nusselt number for the tall cavity simulation at $\mathrm{Ra} = 3.4 \times 10^5$.

- Tolerance parameter for the solution of the velocity and temperature Helmholtz problems, `htol`.
- Tolerance parameter for the solution of the pressure equation, `ptol`.
- Filter parameter, η.

For most of the simulations we performed, the implicit time steps were so short that the errors in the explicit integration of the advective terms were much smaller than any meaningful choice of the integration tolerance `atol`. We have therefore not considered the impact of this parameter on the computed solutions.

4.2.1 Baseline solution

For the baseline solution we consider a series of simulations performed with the the tolerance parameters for the Helmholtz and pressure solvers were both set to strict values `htol` $=$ `ptol` $= 10^{-9}$. We used a regular element grid with $M = 4 \times 20$ elements, and performed spatial and temporal refinement by varying the number of points per element, N, and time step, Δt, respectively.

In Fig. 4.4 we show a typical time history for the global Nusselt number; after the initial transient the flow reaches a statistically steady oscillatory state after about 2500 buoyancy time units, $\tau_0 = \sqrt{\mathrm{Pr}/\nu^2 \mathrm{Ra}}$. Furthermore, Fig. 4.5 shows the instantaneous and fluctuating temperature fields for the final state. Note the skew-symmetry of the solution, the shape and sign of the traveling wave structures are mirrored about the diagonal of the cavity.

We display the spatial and temporal convergence of some key quantities in Figs. 4.6–4.9. In general, both integral and point measures are close to their converged values already at the second coarsest grid, i.e. for $N = 10 \times 10$. The only exception is the mean of the pressure differences – Δp_{14}, Δp_{35}, and Δp_{51} – which are not completely converged even for the

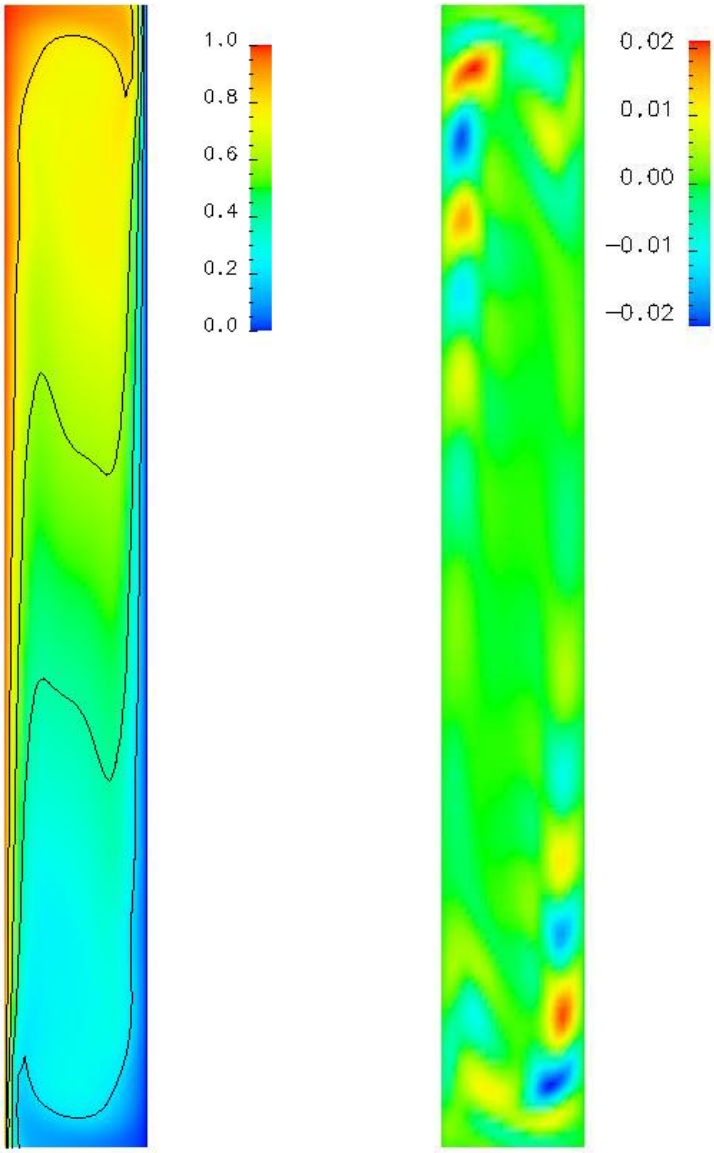

Figure 4.5: Computed instantaneous and fluctuating temperature field for the tall cavity simulation at $\mathrm{Ra} = 3.4 \times 10^5$.

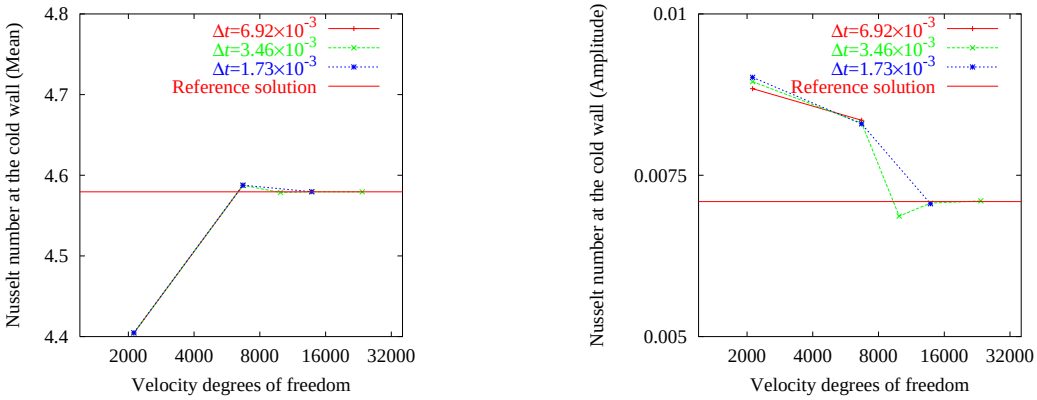

Figure 4.6: Grid convergence for the mean and oscillations amplitude of the hot wall Nusselt number for the tall cavity simulation at $\mathrm{Ra} = 3.4 \times 10^5$.

finest $N = 18 \times 18$ grid. Keep in mind that the pressure discretization is discontinuous across element interfaces, and that the pressure in each element is determined only up to a constant. As this constant may vary from element to element, we can not really expect that the method computes reasonable pressure differences across elements. We can at present only speculate that the overlapping preconditioner, which is based on linear finite elements, provides a weak coupling between the elements such that the computed pressure differences appear to converge slowly to sensible values. We will investigate this issue further and report any conclusions later.

The computations on the coarsest ($N = 6 \times 6$) grid are clearly under-resolved, as can be seen both in the convergence plots and particularly in the time history of the pressure difference shown in Fig. 4.10 in which we see that large spurious pressure spikes contaminate the solution at the coarsest grid. Nevertheless, several of the integral and point measures are fairly well approximated even for this coarse resolution. We see little dependence on the time step in the computed results, this indicates that the temporal resolution sufficient. Note however that we could only use the largest time step on the two coarsest grids because of CFL-like restrictions in the explicit integration of the advective terms.

4.2.2 Dependence on tolerance parameters

We performed a series of simulations in which we varied the numerical tolerance parameters for the iterative solution of the Helmholtz problems for the velocities and temperature, and the pressure operator. We see little dependence on pressure tolerance in the computed results. This is fortunate because the poor conditioning of the pressure operator DQG in (2.7) means that sharpening the pressure tolerance can lead to a significant increase in the iterations needed to converge, and hence in the CPU time required to compute the solution. There is, on the other hand, a definite dependence on the Helmholtz tolerance. In this case, sharpening the tolerance clearly leads to improved solution quality, and this improvement is obtained at reasonable cost as the Helmholtz

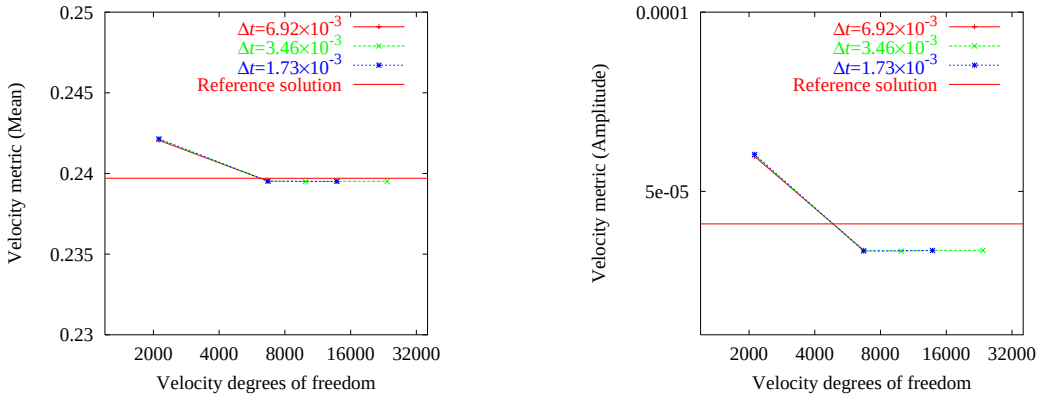

Figure 4.7: Grid convergence for the mean and oscillation amplitude of the velocity metric for the tall cavity simulation at $\mathrm{Ra} = 3.4 \times 10^5$.

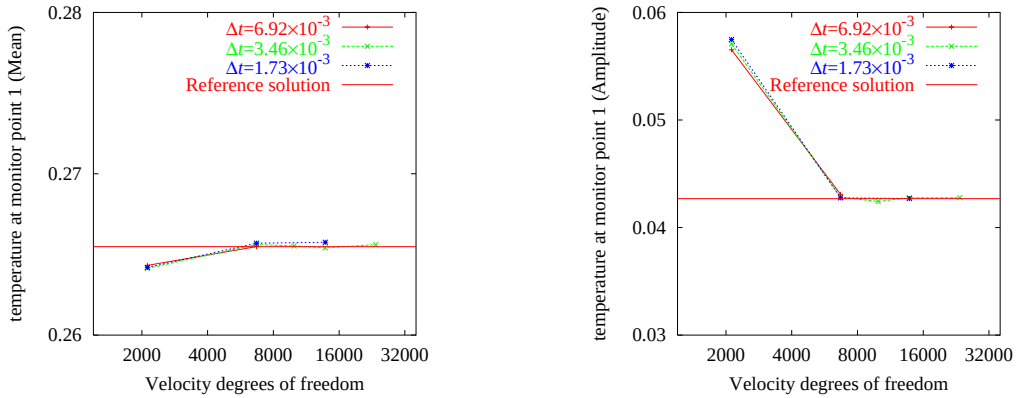

Figure 4.8: Grid convergence for the mean and oscillation amplitude of the point temperature for the tall cavity simulation at $\mathrm{Ra} = 3.4 \times 10^5$.

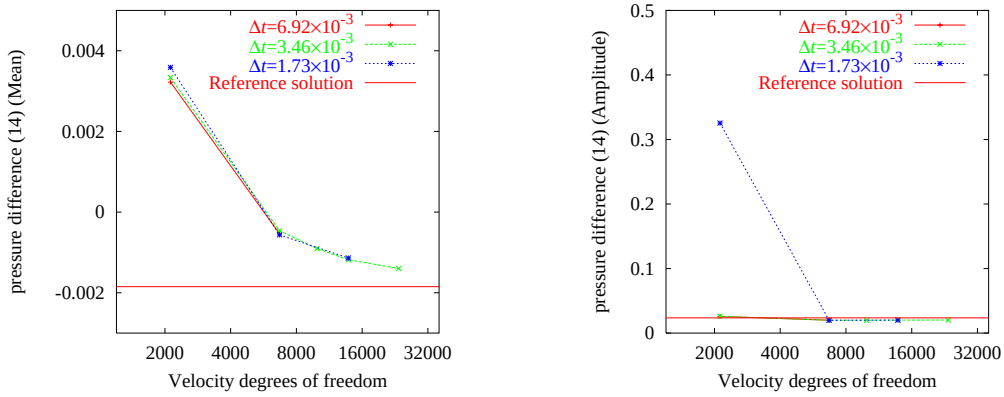

Figure 4.9: Grid convergence for the mean and oscillation amplitude of the pressure difference (Δp_{14}) across the top of the cavity.

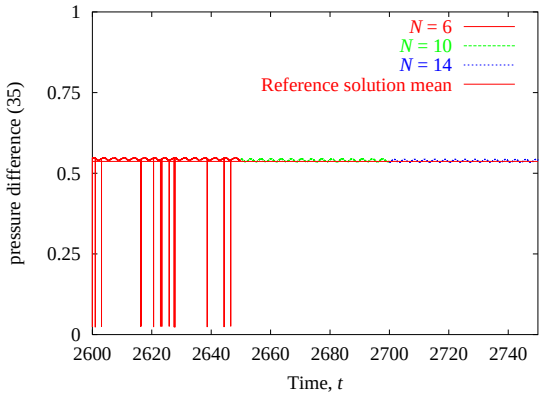

Figure 4.10: Time history of the pressure difference oscillations along the hot wall boundary (Δp_{35}) when the flow is in the statistically steady state.

operators are diagonally dominant and thus converge rapidly Based on these experiments, we arrive at a set of *practical* settings for the tolerance parameters, `htol` $= 10^{-9}$ and `ptol` $= 10^{-6}$, as a reasonable compromise between solution accuracy and efficiency. With these settings both the predicted means and oscillation amplitudes differ from the baseline solution by less than one per cent for all quantities.

4.2.3 The skewness metric

Because of the centro-symmetric property of the base flow, the skewness metric ε_{12} will, in principle, be identically zero for unstable modes that preserve the skew-symmetry. Xin and Le Quéré [19] showed that only one unstable mode exists at the Rayleigh number considered by the benchmark, $\mathrm{Ra} = 3.4 \times 10^5$, and this mode is skew-symmetry preserving.

In all our simulations, the skew-symmetry metric, ε_{12}, oscillates with small mean and amplitude. Two factors appear to contribute to the magnitude of the oscillations. Firstly, and most importantly, the oscillation mean and amplitude depend directly on the Helmholtz tolerance as we show in Fig. 4.11. Reducing `htol` leads to a decrease in ε_{12}. Secondly, the monitor locations do not coincide with the grid points. The solution must therefore be interpolated, and we can detect a small influence of the interpolation errors on ε_{12}. We therefore conclude that ε_{12} is zero within the accuracy of the numerical method, and hence that the computed solutions do indeed preserve the skew-symmetry of the base flow.

4.2.4 Impact of filtering

We can clearly see the importance of controlling the aliasing errors in Fig. 4.12 in which we show the evolution of the velocity metric during the initial transient. For these simulations we used $M = 4 \times 20$ and $N = 10$ which, we have seen above, is sufficient to converge most quantities of interest, in particular the integral measures such as the Nusselt number. If we

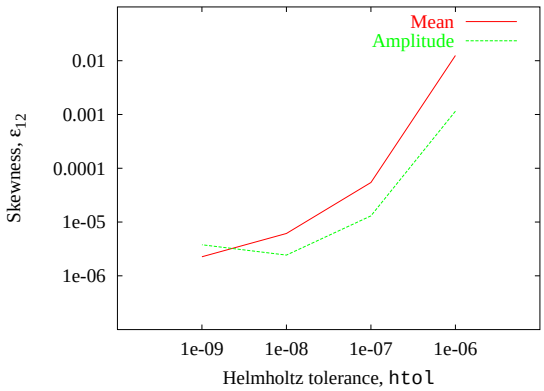

Figure 4.11: Dependence of the skewness metric, ε_{12} on the Helmholtz tolerance parameter, `htol`*, $N = 14$ simulation.*

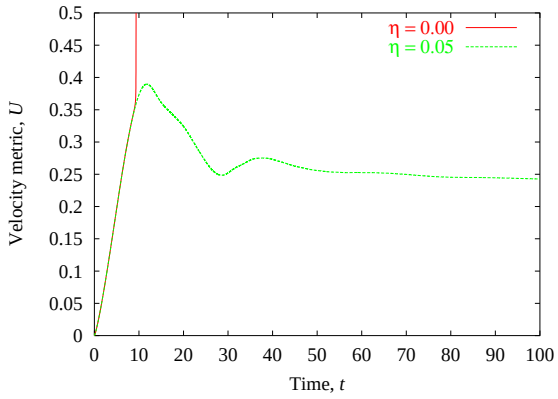

Figure 4.12: Effect of filtering on the time history of the velocity metric, U, during the initial transient.

perform this simulation with no filtering, the kinetic energy blows up early in the transient whereas a small amount of filtering is sufficient to suppress the error growth and to stabilize the simulation. To demonstrate that the filtering does not impact the computed solutions much, we show in Figs. 4.13 and 4.14 that there is no visible dependence on the value of the filter parameter for the oscillations of integral and point values, represented by the global Nusselt number and the temperature, respectively. There is however one notable exception that we show in Fig. 4.15; we can observe a slight increase in the kinetic energy norm with increasing η.

4.2.5 Finally; the benchmark results

Based on the discussion above we present our best shot at the solution, in Table 4.2. As we observed a stronger dependence on spatial than temporal resolution, we use the results from the baseline simulation with $M = 4 \times 20$ elements, $N = 18 \times 18$ points per element,

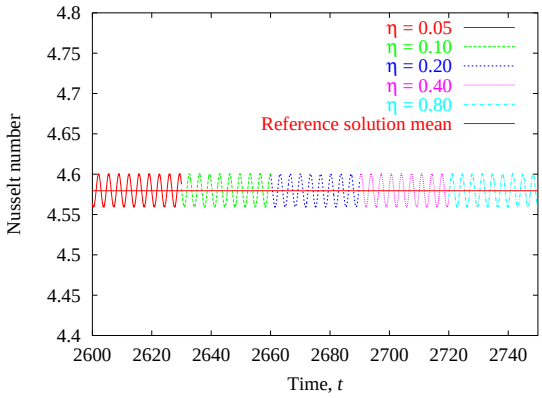

Figure 4.13: Time history of the Nusselt number for different filter parameters, η, when the flow is in the statistically steady state.

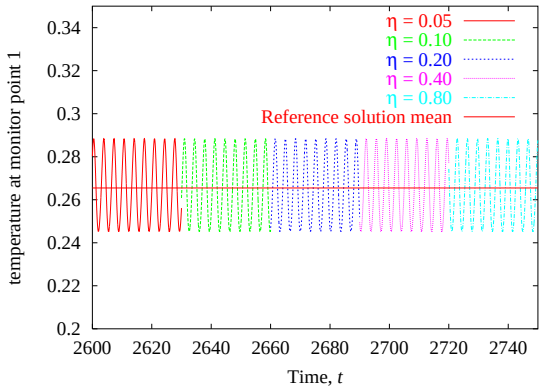

Figure 4.14: Time history of the point temperature for different filter parameters, η, when the flow is in the statistically steady state.

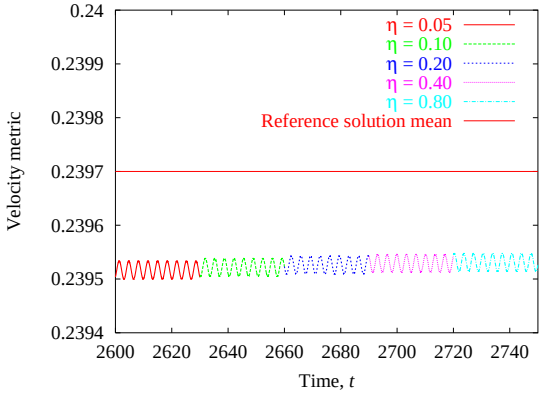

Figure 4.15: Time history of the velocity metric for different filter parameters, η, when the flow is in the statistically steady state.

$\Delta t = 3.46 \times 10^{-3}$, and the filter parameter $\eta = 0.5$ to produce the table. Note that not all the quantities we consider are available in the reference solution provided by Xin and Le Quéré [19]. For these quantities we compare with the average of 29 solutions that were presented at the workshop [3]. For most quantities, the present solution corresponds very well with the reference data with differences less than one per cent. There are some exceptions though; we under-predict for example the oscillation amplitude for the centre-line Nusselt number with a factor of almost ten. The pressure difference across the top of the cavity, Δp_{14}, is not fully converged as we saw in Fig. 4.9, and this explains at least in part the large deviations in the mean values for this quantity. For some of the other quantities for which we have large deviations, such as the velocity metric amplitude and the point vorticity data, the predictions are nevertheless well within the scatter of the available solutions. The predicted stream function data are however wide off the mark compared to the other solutions. We do not at present know the reason for this discrepancy.

References

[1] G. de Vahl Davis. Natural convection in a square cavity: A bench mark numerical solution. *Int. J. Numer. Meth. Fluids*, 3:249–264, 1983.

[2] M. Hortmann, M. Perić, and G. Scheurer. Finite volume multigrid prediction of laminar natural convection: Bench-mark solutions. *Int. J. Numer. Meth. Fluids*, 11:189–207, 1990.

[3] M. A. Christon, P. M. Gresho, and S. B. Sutton. Computational predictability of time-dependant natural convection flows in enclosures (including a benchmark solution). *Int. J. Numer. Meth. Fluids*, 40:953–980, 2002.

[4] P. F. Fischer and J. S. Mullen. Filter-based stabilization of spectral element methods. *Comptes Rendus de l'Académie des sciences Paris, t.332, Série I - Analyse numérique*, pages 265–270, 2001.

[5] Y. Maday, A. Patera, and E. M. Rønquist. An operator-integration-factor method for time-dependent problems: Application to incompressible fluid flow. *J. Sci. Comput.*, 4:263–292, 1990.

[6] A. T. Patera. A spectral element method for fluid dynamics: Laminar flow in a channel expansion. *J. Comput. Phys.*, 54:468–488, 1984.

[7] Y. Maday and A. T. Patera. Spectral element methods for the incompressible Navier–Stokes equations. In A. K. Noor and J. T. Oden, editors, *State-of-the-Art Surveys on Computational Mechanics*, chapter 3. ASME, 1989.

[8] P. F. Fischer. Private communication, May 2002.

[9] R. M. Kirby and G. E. Karniadakis. De-aliasing on non-uniform grids: algorithms and applications. *J. Comput. Phys.*, 191:249–264, 2003.

Table 4.2: Computed diagnostic quantities for the simulation of a tall cavity at $\mathrm{Ra} = 3.4 \times 10^5$.

	$\overline{\mathrm{Nu}_0}$	Nu_0'	$\overline{\mathrm{Nu}_{\mathrm{cl}}}$	$\mathrm{Nu}_{\mathrm{cl}}'$
Present results:	4.57943	7.1026e-2	4.57947	0.01669
Reference:	4.57946	7.0918e-2	4.57946	0.17761
Difference (%):	0.0007	0.127	0.0002	90.607

	$\overline{U}$†	U'†	$\overline{\Omega}$†	Ω'†
Present results:	0.2395	3.354e-5	3.0171	3.198e-3
Reference:	0.2397	4.093e-5	2.9998	3.488e-3
Difference (%):	0.078	18.05	0.576	8.302
Difference (σ):	0.188	0.608	0.223	0.679

	$\overline{u_1}$	u_1'	$\overline{v_1}$	v_1'
Present results:	5.6220e-2	5.4880e-2	0.46173	7.7726e-2
Reference:	5.6356e-2	5.4828e-2	0.46188	7.7123e-2
Difference (%):	0.228	0.178	0.033	0.149

	$\overline{\theta_1}$	θ_1'	τ_θ	
Present results:	0.265612	4.2774e-1	3.4109	
Reference:	0.265480	4.2740e-2	3.4115	
Difference (%):	0.050	0.199	0.018	

	$\overline{\psi_1}$†	ψ_1'†	$\overline{\omega_1}$†	ω_1'†
Present results:	−4.598e-2	4.324e-4	−2.3677	1.0801
Reference:	−7.249e-2	7.864e-4	−2.2845	1.2325
Difference (%):	36.6	94.5	3.64	12.5
Difference (σ):	7.77	4.437	0.578	0.502

	$\overline{\Delta p_{14}}$	$\Delta p_{14}'$	$\overline{\Delta p_{35}}$	$\Delta p_{35}'$
Present results:	−1.14e-3	2.023e-2	0.5376	0.999e-2
Reference:	−1.8536e-3	2.0355e-2	0.53671	1.0056e-2
Difference (%):	24.5	0.600	0.164	0.68

†: Some quantities were not provided in the solution presented in [19]. For these quantities the reference values are the average of 29 solutions presented at the workshop [3], and we also present the differences in terms of the standard deviations of the contributed solutions.

[10] A. J. Chorin. Numerical solution of the Navier-Stokes equations. *Math. Comp.*, 23:351–354, 1968.

[11] J. Van Kan. A second-order accurate pressure-correction scheme for viscous incompressible flow. *SIAM J. Sci. Stat. Comput.*, 7:870–891, 1986.

[12] J. Blair Perot. An analysis of the fractional step method. *Journal of Computational Physics*, 108:51–58, 1993.

[13] W. Couzy. *Spectral element discretization of the unsteady Navier-Stokes equations and its iterative solution on parallel computers*. PhD thesis, École Polytechnique Fédérale de Lausanne, 1995. Thèse No. 1380.

[14] P. F. Fischer, N. I. Miller, and F. M. Tufo. An overlapping Schwarz method for spectral element simulation of three-dimensional incompressible flows. In P. Bjørstad and M. Luskin, editors, *Parallel Solution of Partial Differential Equations*. Springer-Verlag, 2000.

[15] G. I. Taylor. On the decay of vortices in a viscous fluid. *Philos. Mag.*, 46:671–674, 1923.

[16] C. R. Ethier and D. A. Steinman. Exact fully 3D Navier-Stokes solutions for benchmarking. *Int. J. Numer. Meth. Fluids*, 19:369–375, 1994.

[17] A.E. Gill. The boundary-layer regime for convection in a rectangular cavity. *J. Fluid Mech.*, 26:515–536, 1966.

[18] G. de Vahl Davis and I. P. Jones. Natural convection in a square cavity: A comparison exercise. *Int. J. Numer. Meth. Fluids*, 3:227–248, 1983.

[19] S. Xin and P. Le Quéré. An extended Chebyshev pseudo-spectral benchmark for the 8:1 differentially heated cavity. *Int. J. Numer. Meth. Fluids*, 40:981–998, 2002.